JOURNAL OF SPACECRAFT AND ROCKETS
Vol. 31, No. 4, July–August 1994

Computation of Unsteady Flow past an Oscillating Cylinder near a Vertical Wall

Guan-Wei Yen* and Oktay Baysal†
Old Dominion University, Norfolk, Virginia 23529

Some flowfields involve multiple bodies with at least one of the components in relative motion with respect to the others. Because of the inherent dynamic interference, the generated unsteady flowfield displays features significantly different than that around a static body. With this motivation, a computational method called kinematic domain decomposition is developed to simulate an unsteady flow past moving bodies and their aerodynamic interference. The inviscid equations governing the flowfield and the dynamics equations governing the rigid-body motion are solved simultaneously on decomposed computational domains. The subdomain grids can move with respect to and communicate with each other. Initially, the method is validated by comparing its results with the experimental data for a pitching airfoil. Then, the method is demonstrated for flows past a cylinder that is pitched sinusoidally near a static vertical wall. The results indicate a stronger interference for a subsonic flowfield than a supersonic flowfield. By contrasting these dynamic flowfields with that of a static cylinder, effects of the dynamics on the interference features are shown. It is concluded that performing a number of sequential steady-state computations is not adequate for a flowfield around an object in relative motion near another object.

Nomenclature

a_∞	= freestream speed of sound
C_A	= axial force coefficient
C_N	= normal force coefficient
C_{mp}	= pitching moment coefficient
C_{my}	= yawing moment coefficient
C_p	= pressure coefficient
d	= cylinder diameter, 50.8 mm
E_1, E_2, E_3	= inviscid flux vectors
e_t	= total energy
G_j	= jth subdomain grid
J	= Jacobian matrix of transformation
k	= reduced frequency, $\omega L/2V_\infty$
L	= reference length, 12.47d
M_∞	= freestream Mach number
p	= pressure
p'	= normalized pressure fluctuation
Q	= vector of conserved variables
Re	= Reynolds number
t	= time
U_j	= jth contravariant velocity component
u_j	= jth velocity component
V_∞	= freestream velocity
x_j	= jth Cartesian coordinate
α	= angle of attack
γ	= ratio of specific heats
ξ^j	= jth generalized curvilinear coordinate
ρ	= density
ω	= frequency, Hz
$\downarrow\uparrow$	= up and down motions, respectively

Introduction

ALTHOUGH the majority of computational flow analyses performed to date have involved steady flows about stationary bodies, most of the physically realistic flow problems are actually unsteady in character. Furthermore, most unsteady flows involve multiple bodies with at least one of them in relative motion with respect to the others. Typical examples of these unsteady flows include the periodic motion or random vibration of aircraft wings, rotor-stator interactions in turbomachinery, relative motion of propeller blades, relative motion of flaps, store separation from an aircraft,[1,2] and solid-rocket-booster separation from the Space Shuttle. Because of interference, the generated unsteady flowfield often displays features significantly different than that past a static body.

Simulating the body motion and the related unsteady flowfield as a number of sequential steady-state flow computations[1,2] sometimes may provide an adequate solution. However, freezing the body motion during each steady-state computation may lead to erroneous predictions, particularly for a case where the motion-induced flow component is not negligible. As reported in Ref. 3, for example, the unsteady and steady computations for a sinusoidally pitching airfoil have resulted in unacceptably different flowfield predictions.

For the class of unsteady problems which involve only a single body experiencing a rigid-body motion, at least three different solution methods have been reported.[4–6] However, for unsteady flow problems that involve multiple bodies, it is rather difficult to generate these single-domain grids and to solve the governing equations as the objects move with respect to each other.

The present extension of the two-dimensional kinematic domain decomposition (KDD) method[3] aims at solving such three-dimensional problems with a higher degree of accuracy. Time-dependent Jacobian metrics are used to transform the moving physical domain to the static computational domain. Thus, the method intends to achieve the following: 1) simulate the flowfield about three-dimensional moving multiple bodies and their aerodynamic interference, 2) reduce the dispersion error, which strongly affects the propagation of gasdynamic waves between the objects, and 3) reduce the phase error that accumulates with the numerical time-advancing procedure.

Mathematical Formulation

The governing equations of the fluid motion are the three-dimensional, compressible, time-dependent Euler equations,

$$\frac{\partial \mathbf{Q}}{\partial t} + \frac{\partial \mathbf{E}_m}{\partial \xi^m} = 0 \tag{1}$$

where m is the dummy index and $\mathbf{Q}$ is the vector of conserved variables,

$$\mathbf{Q} = [\rho, \rho u_1, \rho u_2, \rho u_3, e_t]^t / J \tag{2}$$

Presented as Paper 92-4653 at the AIAA Atmospheric Flight Mechanics Conference, Hilton Head, SC, Aug. 10–12, 1992; received Nov. 9, 1992; revision received March 26, 1993; accepted for publication March 31, 1993.

*Graduate Research Assistant, Aerospace Engineering Department. Senior Member AIAA.

†Professor, Aerospace Engineering Department. Senior Member AIAA.

The inviscid fluxes are denoted by

$$\mathbf{E}_m = \frac{1}{J}[\rho U_m, \rho u_1 U_m + \partial_1 \xi^m p, \rho u_2 U_m + \partial_2 \xi^m p,$$

$$\rho u_3 U_m + \partial_3 \xi^m p, U_m(e_t + p) - \xi_t^m p]^t \tag{3}$$

These equations are written in strong conservation form and in the time-dependent, curvilinear coordinates,

$$\xi^m = \xi^m(x_1, x_2, x_3, t) \tag{4}$$

The contravariant velocities are

$$U_m = \partial_k \xi^m u_k + \partial_t \xi^m \tag{5}$$

The air is assumed to be a perfect gas with the state equation given as

$$p = \rho(\gamma - 1)\left(e^t - \frac{u_1^2 + u_2^2 + u_3^2}{2}\right) \tag{6}$$

All the variables are normalized using the reference length (cylinder plus sting), the freestream density, and the freestream speed of sound.

Solution Algorithm

The finite-volume differencing of Eq. (1) is formulated by integrating over a stationary control volume,

$$\frac{\partial}{\partial_t}\int_V \mathbf{Q}\,dV + \int_s \mathbf{E}\cdot\mathbf{n}\,ds = 0 \tag{7}$$

where $\mathbf{n}$ is the unit normal vector pointing outward from the surface s bounding the volume V.

Equation (7) is solved using a temporally and spatially second-order-accurate algorithm. Roe flux-difference splitting[7] is used to construct the upwind-biased differences of the spatial derivatives. Equation (1) is integrated in time using the Euler backward formula. After the approximate factorization for this alternating-direction implicit (ADI) method, the solution is achieved by 5×5 block-tridiagonal matrix inversions in each of the three directions. The delta form of this method is given below:

$$\left\{\frac{I}{J\Delta t} + \frac{\theta}{1+\alpha}\left[\Delta_{\xi^1}\left(\partial_{\mathbf{Q}} E_1\right)\right]\right\}$$

$$\times\left\{\frac{I}{J\Delta t} + \frac{\theta}{1+\alpha}\left[\Delta_{\xi^2}\left(\partial_{\mathbf{Q}} E_2\right)\right]\right\}$$

$$\times\left\{\frac{I}{J\Delta t} + \frac{\theta}{1+\alpha}\left[\Delta_{\xi^3}\left(\partial_{\mathbf{Q}} E_3\right)\right]\right\}\Delta\mathbf{Q}^n$$

$$= \frac{1}{1+\alpha}\left[\Delta_{\xi^1}(-\mathbf{E}_1)^n + \Delta_{\xi^2}(-\mathbf{E}_2)^n + \Delta_{\xi^3}(-\mathbf{E}_3)^n\right]$$

$$+\frac{\alpha}{1+\alpha}\Delta\mathbf{Q}^{n-1} + \vartheta\left[\left(lf + \theta - \tfrac{1}{2} - \alpha\right)\Delta t^2, \Delta t^3, \Delta x_j^3\right] \tag{8}$$

where $\Delta\mathbf{Q}^n = \mathbf{Q}^{n+1} - \mathbf{Q}^n$. The last term in Eq. (8) indicates the order of magnitude of the leading truncated term. The method is second-order accurate in space. The temporal accuracy, however, depends on the magnitude of the neglected terms in linearization and in approximate factorization (represented by the parameter lf), as well as the values of the free parameters α and θ. For $\alpha = 1/2$ and $\theta = 1$, the temporal truncation error becomes $\vartheta(lf \cdot \Delta t^2, \Delta t^3)$. For the cases where the second-order flux Jacobians and the product of the first-order flux Jacobians are small, lf tends to vanish. That is, the method approaches temporal second-order accuracy.[8]

Details and the implementation of this computational fluid dynamics (CFD) method can be found in the following references: the baseline method in Ref. 7, the higher-order unsteady method in Refs. 3 and 8, and its extension to multiple domains in Refs. 2 and 9.

As a result of the discretization procedure used in any given numerical scheme, the unsteady flow effectively propagates in a dispersive medium. However, for unsteady flow computations, the phase error becomes just as important as the dissipation error. In addition, since the solution develops time-accurately for an unsteady flow (rather than converging as it does for a steady solution), the phase error continues to accumulate. Consequently, the group velocity of the motion may deviate significantly from its phase velocity.

As it is reported in Ref. 10, when the one-dimensional, linearized, inviscid equations are discretized with an upwind-biased scheme and the Courant number is kept between zero and one, the numerical solution may be essentially free of dispersion. It should be noted that the approximate factorization introduces an additional dispersion. Nonetheless, other investigations, such as Refs. 8 and 11, also conclude that a second-order accurate ADI scheme with the Roe's modification should adequately capture the unsteady flow and the associated wave motion. Hence, the present CFD method is justified for unsteady computations, and the maximum Courant number is kept under unity.

The discretized flow equations are solved on a grid system known as the composite grid. A composite grid for the flow domain may consist of any combination of multiblock grids, degenerate zonal grids, zonal grids, and overlapped grids. Moreover, these subdomain grids may be in relative motion with respect to the other subdomain grids.[3]

For the present applications, three-dimensional, overlapped, and moving grids are employed. The static overlapped-grid algorithm reported in Ref. 12 is extended to serve for a finite-volume, upwind CFD algorithm that can simulate flows past dynamic bodies. Such an extension is also reported in Ref. 13. The motion of each subdomain grid is accounted for by the time-dependent curvilinear coordinate transformations [Eqs. (3–5)], whereby the grid velocities are also determined. The grid speed is computed by

$$\partial_t \xi^m = -\partial_k \xi^m \frac{\partial x_k}{\partial t} \tag{9}$$

The intergrid information transfer (connectivity) is time-dependent. That is, all the connectivity searches, the bookkeeping for the interpolations, and other modes of transfer are renewed and updated as functions of time.

Two important concerns in developing the present KDD method are its accuracy and efficiency. The KDD method has several advantages in this regard. First, a subdomain and its cells are not deformed; therefore, the geometric conservation (Jacobian transformation) can be preserved.[14] Second, this method can calculate unlimited subdomains, and each subdomain may move independently of the others. Third, since the governing equations are written in the space-fixed frame of reference, all the primitive variables are absolute everywhere and at any time, irrespective of the subdomain grid on which they are computed. Therefore, they can be transferred from one subdomain to another regardless of the relative motion between them. Finally, KDD may conceivably allow using different approximations of the flow equations and different solution techniques in different subdomains. Some details of this method, albeit in two dimensions, can be found in Ref. 3.

Although the solution algorithm is implicit, the boundary conditions are specified explicitly. Their treatment depends on the flow regime and the type of grid used. On the vertical solid wall (Fig. 2), the normal gradients of pressure and density are assumed to be zero, and the normal contravariant velocity is set equal to zero. For subsonic flows, the remaining boundaries of the Cartesian grid (i.e., top, bottom, inflow, outflow, and far-field) are determined using the characteristic boundary conditions.[15] However, for supersonic flows, the inflow boundary of the Cartesian grid is fixed at the freestream conditions, and the outflow Cartesian boundary is determined by a simple first-order extrapolation from the interior grid cells.

The wake-cut planes of the C-O grid are treated by averaging the property values from both sides of the cut. The downstream of the C-O grid is determined using the characteristic boundary conditions. For the surface of the cylinder, solid-wall boundary conditions similar to those used for the vertical wall are employed. Since the cylinder is in motion, the grid speed is added to the contravariant

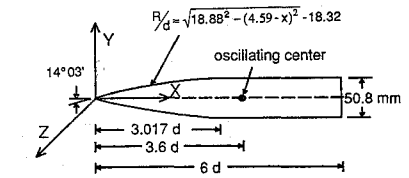

a)

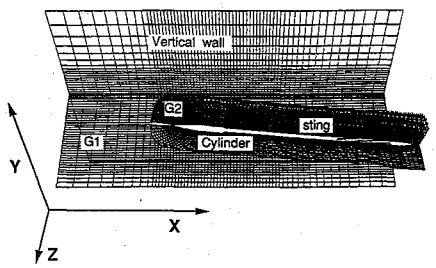

b)

Fig. 1 a) Geometric definition of the secant-ogive-cylinder (SOC) and b) composite grid for SOC near a vertical wall.

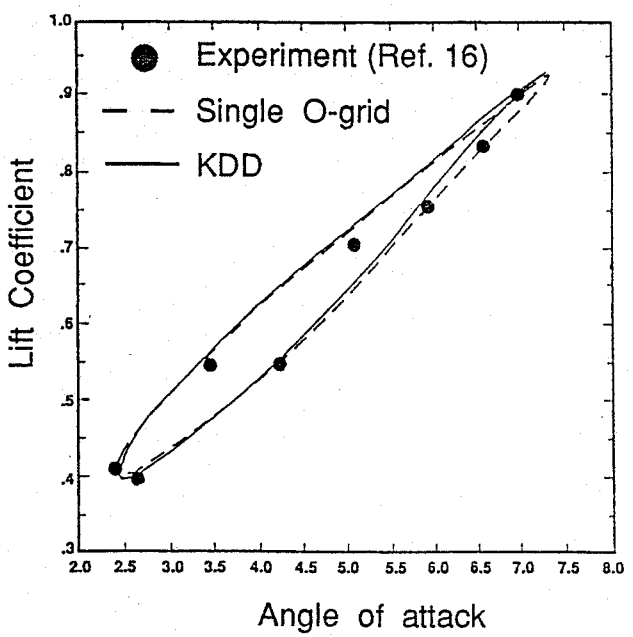

Fig. 2 Lift coefficient versus the angle of attack for one cycle of a sinusoidally pitching NACA 0012 airfoil.

velocities. The portion of the outer C-O boundary that becomes an intergrid boundary (and consequently does not coincide with the physical boundaries) is updated by the intergrid communication. The type of intergrid boundary conditions depends on the type of domain decomposition (either static or dynamic) used in that boundary. In the rear portion of the sting, which is not overlaid within the Cartesian grid, the characteristic boundary conditions are employed.

Computational Cases

The computational method is demonstrated by considering the secant-ogive cylinder (SOC) defined in Fig. 1a. The cylinder is placed $4d$ away from a vertical wall in order to form a multiple body configuration, and it is forced to pitch in a plane (X-Y) parallel to the wall (Fig. 1b). Prior to presenting the demonstrative cases, however, two issues have to be addressed: namely, the validation of the KDD method and the adequacy of the grid shown in Fig. 1b.

Unfortunately, accurate and reliable experimental data for the dynamic SOC (Fig. 1a) could not be found for the validation. Hence, the subsonic flow ($M_\infty = 0.6$) past a pitching ($\omega = 50.32$ Hz, $k = 0.162$) NACA 0012 airfoil is simulated using the present KDD method. The composite grid consists of a pitching O grid overlapped on a fixed Cartesian grid. Displayed in Fig. 2 are the comparisons of the KDD computations with the experimental data.[16] These results are also compared with those obtained by the present CFD method but using a single O grid, that is, without KDD. The results agree with each other fairly well. Observed discrepancies during the pitchdown may be attributed to the nonconservative flux transfers across the overlapped grids in time.[1,2,12,13] Details of this validation case can be found in Ref. 3. The grid independence issue will be discussed along with the results of case 1.

Table 1 Description of the computational cases

Case	Mode	M_∞	α_0, deg	α_1, deg	k	ω, Hz
1.a,1.b	Static	0.7		0	0	0
2	Pitching		7.5		0.3	36.5
3		1.8		10.0	0.2	62.6

Table 2 Computational details

Case	Grid size	CPU time per step per cell, μs	CPU time per cycle, h	Time step, ms	Time steps per cycle
1.a	482,012				
1.b		14.0	—[a]		—[a]
2	196,370		46.8	0.4	52,360
3		16.4	70.0		78,540

[a]Not applicable.

Three cases are reported in the present paper (Table 1). The cylinder is kept stationary in the first case, so that a means of contrasting the dynamic effects is established. The second and third cases are designed to investigate the unsteady flowfields generated by the cylinder experiencing the prescribed pitching motion. This forced motion is described by the following time function α:

$$\alpha(t) = \alpha_0 + \alpha_1 \sin(kt) \tag{10}$$

To study the effect of the flow regime, the freestream is chosen to be subsonic in the second case and supersonic in the third case.

The composite grid consists of two subdomains (Fig. 1b). The cylinder subdomain is discretized by a C-O grid, which is $7d$ in diameter and $30d$ long, and has its local origin $4d$ away from the vertical wall. The wall subdomain is discretized by a stretched Cartesian grid, which has a length, width, and height of $41d$, $30d$, and $30d$, respectively (Fig. 1b). Then the C-O grid is overlapped on the Cartesian grid. There are $70 \times 31 \times 21$ points in the C-O grid and $65 \times 40 \times 58$ points in the Cartesian grid (Fig. 1b). To study the grid dependence of the solution, a much finer grid is also constructed with $97 \times 41 \times 28$ points in the C-O grid and $88 \times 54 \times 78$ points in the Cartesian grid (Table 2). As can be discerned from Fig. 3, the case 1b solution is sufficiently close the one obtained on the finer grid for case 1a, yet it is obtained at a much lower computational cost. Since this cost difference would be prohibitive for the unsteady, dynamic cases, where the calculations must be performed time-accurately, cases 2 and 3 are computed on the grid with 196,370 cells.

Shown in Table 2 are some of the computational details. The normalized CPU time (CPU per time step per cell) for case 2 is greater than that of case 1. Most of this extra time is needed for the time-dependent KDD connectivity and information transfer operations, and a small portion of it is for the computations of rigid-body motion.

In case 2, the grid and the freestream flow conditions are identical to those of case 1, but the cylinder and its C-O grid are forced to pitch sinusoidally. Therefore, the converged solution of case 1 is used as the initial conditions for case 2; then the computations are performed time-accurately for two cycles. The solution for the first cycle is discarded to reduce the effects of the numerical transients on the final solution. In addition, some of this first cycle time is needed for the cyclic boundary-motion-induced flow component to

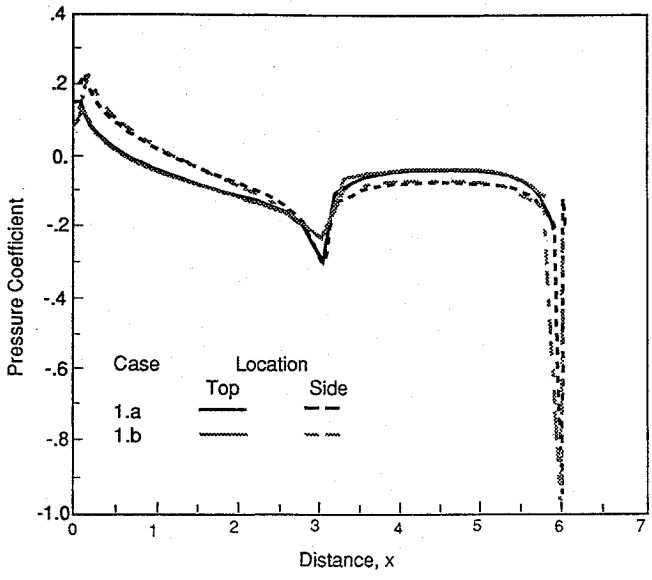

Fig. 3 A grid refinement study for case 1. Pressure coefficient distributions along the top and the side of the cylinder using a finer grid (case 1a) and the regular grid (case 1b).

develop. That is, due to the inertia of a fluid particle, its response to the rigid-body motion requires some lag time.

Results

The converged solution for the steady flow past the static SOC (case 1) is obtained using local time steps with the global Courant number limited to unity. Shown in Figs. 4a and 4b are the normalized pressure contours on the vertical wall and the symmetry plane of the cylinder, respectively. It can be observed that only minor aerodynamic interference between the two objects is present, with the maximum p' value of -0.006 occurring on the wall. The subsonic flow is initially compressed on the top surface; then it gradually expands toward the tail of the cylinder. An expansion wave can be seen on the bottom surface being terminated by a weak shock.

The normalized pressure contours of case 2 at 7.5 deg ↑ angle of attack are shown in Figs. 5a and 5b. To facilitate some qualitative comparison between Figs. 4 and 5, they are plotted for the corresponding planes at the identical locations. The maximum p' value of 0.05 can be observed on the wall (Fig. 5a); it is an order of magnitude greater than that of the stationary cylinder at the same angle of attack. Also, the gasdynamic compression and expansion regions are switched in their locations as compared with case 1. The shift in the contour locations (Fig. 5b) toward the far field indicates the formation of a lower-pressure zone between the two objects. This may be attributed to interference as well as the increased relative speed between the moving cylinder and the flow.[3]

The aerodynamic coefficients for cases 1 and 2 are presented in Figs. 6a and 6b. Note that the definition of all the aerodynamic coefficients follows the right-hand rule. C_A and C_N are defined to be along and perpendicular to the cylinder axis, respectively. C_{mp} is in the plane parallel to the vertical wall (X-Y), and C_{my} is in the X-Z plane.

The computed aerodynamic coefficients are very close to zero for the static cylinder in case 1. However, for the dynamic cylinder in case 2, C_A is always greater than zero and displays peaks at the upper and lower extremes of α (Fig. 6a). C_N does not appear to be proportional to α; rather it displays sudden changes near the α value at which the pitching motion transitions to the opposite direction. Note that as the cylinder pitches up from 0 to 15 deg, the value of C_N remains negative, but it suddenly changes its sign at 15 deg, which corresponds to the peak value of C_A. A similar phenomenon is observed during the pitchdown motion.

C_{mp} corresponds well to the cylinder's pitching motion (Fig. 6b). For example, when the cylinder pitches up from -2 to 17 deg, the value of C_{mp} is always negative. This indicates that the aerodynamic forces are assisting in raising the cylinder's nose with respect to the oscillation center. The C_{my} history displays only minor fluctuations throughout the cycle, and it only takes negative values. In other words, the cylinder's nose is constantly pushed in towards the vertical wall, but its tail is pushed away from the wall.

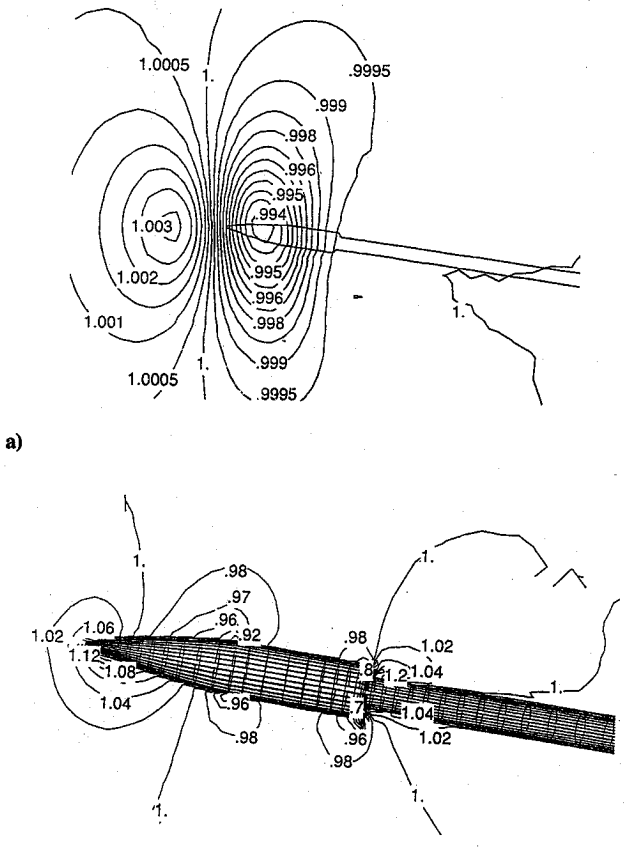

Fig. 4 Normalized pressure contours for case 1b: a) on the wall and b) on the symmetry plane of the static cylinder at $\alpha = 7.5$ deg.

The same subdomain grids and connectivity information used for case 2 are also used for case 3, where the freestream flow is supersonic. Again, computations are performed time-accurately for two cycles. Shown in Figs. 7a and 7b are the instantaneous normalized pressure contours at 17.3 deg ↑, which are plotted at exactly the same planes as those for cases 1 and 2. Shown in Fig. 7b is the cross section of a three-dimensional conical shock attached to the cylinder tip. The shock is weaker along the upper surface and stronger along the lower surface of the cylinder. The flow expands around the cylinder's base. Comparing Figs. 7a and 7b, it can be seen that the conical shock generated at the nose of cylinder impinges on the vertical wall. The pressure values on the wall are almost proportional to the strength of the shock about the cylinder, that is, weaker above the cylinder and stronger below the cylinder.

The aerodynamic coefficients for case 3 are shown in Fig. 8. C_A is always positive, with a maximum between 4 and 8 deg during the pitchup motion. C_N remains positive during the pitchup motion, but suddenly becomes negative during the pitchdown motion. The pitching moment corresponds well to the cylinder's pitchup motion. During the pitchdown motion, such a correspondence is observed from 12.5 to 17.5 deg and from -2.5 to 1.0 deg. Unlike the subsonic flow of case 2, the yawing moment is zero for the entire motion of case 3. This is predominantly due to the fact that the nose shock reflecting off the wall impinges on the sting and not on the cylinder. Since the force calculations are performed for the cylinder only, and since the upstream is not affected by the downstream in inviscid, supersonic flows, the yawing moment is not influenced by the interference occurring in case 3.

Shown in Figs. 9a and 9b are the instantaneous normalized pressure contours at 17.3 deg ↓, which are plotted at the same planes as

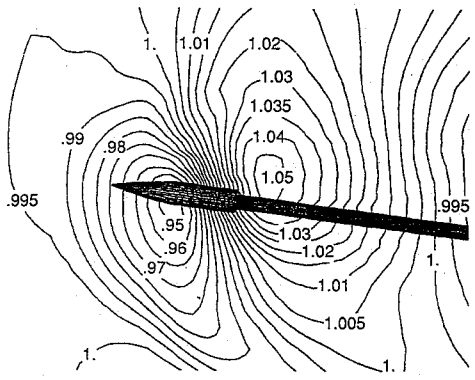

a)

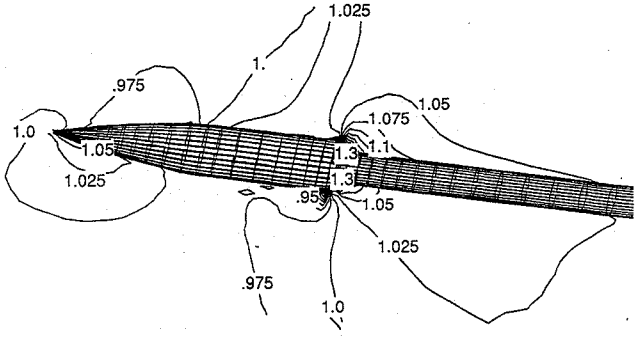

b)

Fig. 5 Normalized pressure contours for case 2 during the pitchup motion at $\alpha = 7.5$ deg ↑: a) on the wall and b) on the symmetry plane of the sinusoidally pitching cylinder.

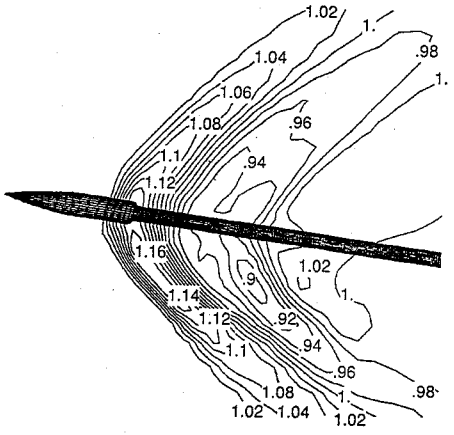

a)

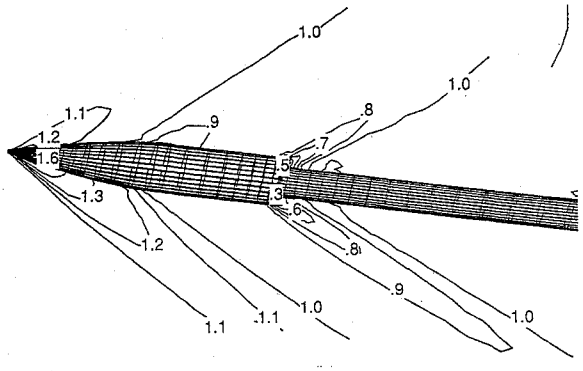

b)

Fig. 7 Normalized pressure contours for case 3 during the pitchup motion at $\alpha = 17.3$ deg ↑: a) on the wall and b) on the symmetry plane of the sinusoidally pitching cylinder.

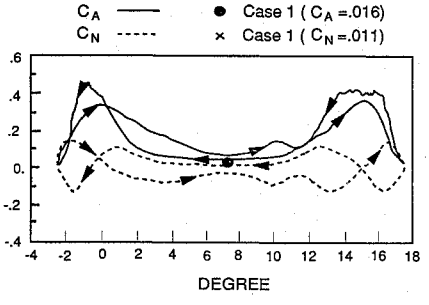

a)

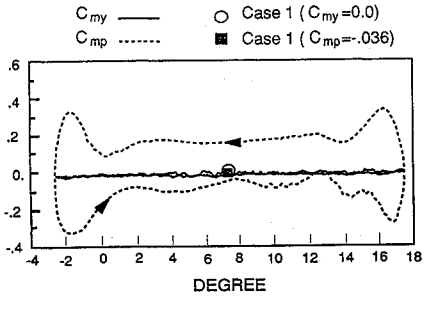

b)

Fig. 6 Aerodynamic coefficients versus the angle of attack for one cycle of a sinusoidally pitching cylinder for case 2: a) force coefficients and b) moment coefficients. Positive C_{mp} and C_{my} push the nose down and away from the wall, respectively.

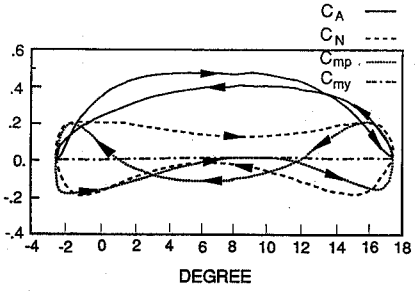

Fig. 8 Aerodynamic coefficients versus the angle of attack for one cycle of the sinusoidally pitching cylinder for case 3.

those of Figs. 7a and 7b. They are intended to show the differences in the response of the flow to the pitchup and the pitchdown motions of the cylinder.

Comparing Figs. 7b (pitchup) and 9b (pitchdown), it can be observed that the stronger shock located along the bottom surface during the pitchup motion is switched to the top surface during the pitchdown motion. The higher pressure values along the bottom surface seen in Fig. 7b generate the positive normal force seen in Fig. 8. Conversely, the pitchdown motion (Fig. 9b) causes a negative normal force. The shock interference between the two bodies can be observed from Figs. 7a and 9a. During the pitchup motion, the stronger shock is located along the bottom surface, which in turn impinges on the vertical wall. Hence, the higher pressure values can be seen on the lower portion of the wall in Fig. 7a. However, during the pitchdown motion, the stronger shock is along the top surface,

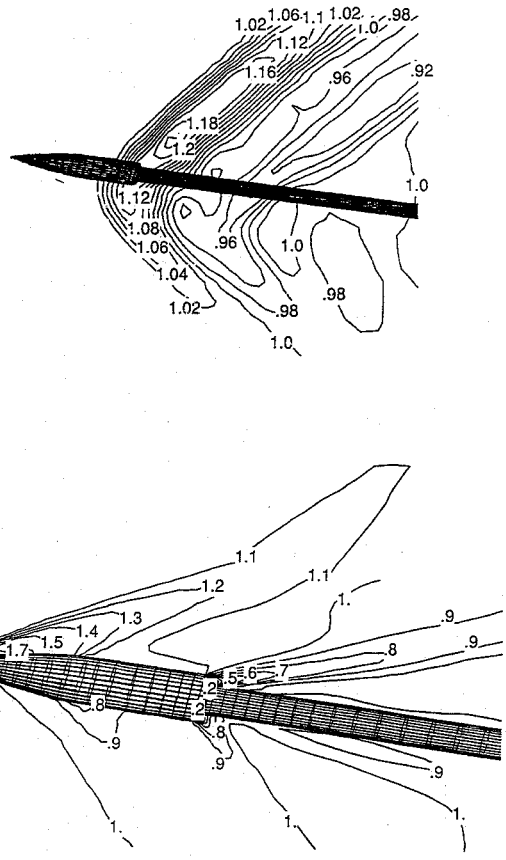

a)

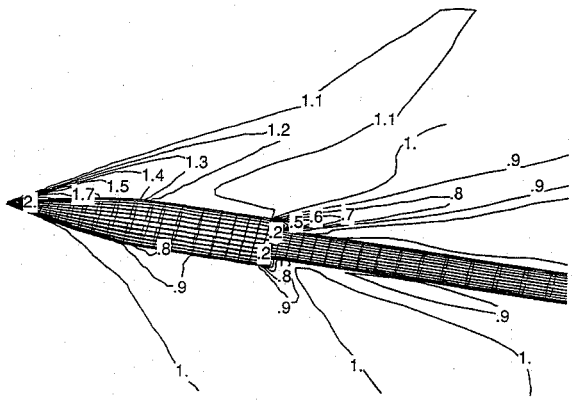

b)

Fig. 9 Normalized pressure contours for case 3 during the pitchdown motion at $\alpha = 17.3$ deg ↓: a) on the wall and b) on the symmetry plane of the sinusoidally pitching cylinder.

which causes the higher pressure values on the upper portion of the vertical wall (Fig. 9a).

Conclusions

A three-dimensional method is developed to computationally simulate an unsteady flow past multiple bodies engaged in a relative motion. The method employs a composite of subdomain grids, which are independently generated. The flow equations are solved using the time-dependent, generalized coordinates in the absolute frame of reference. The values of the primitive flow variables are directly transferred across the grid interfaces. The method is validated by comparing its two-dimensional results with experimental data.

The kinematic domain decomposition (KDD) method is demonstrated through the three-dimensional subsonic and supersonic flow simulations of a cylinder pitching sinusoidally in the proximity of a vertical wall. An advantage of KDD is that each subdomain and its local origin can be defined independently. Hence, this method has the capability to resolve the aerodynamics of various unsteady problems involving the relative motion of multiple bodies.

The demonstrative results for a subsonic case indicate strong interference between a pitching cylinder and a static wall. For a supersonic case, the reflected shock wave does not interact with the cylinder, but it impinges on its sting at the distance at which it is positioned from the wall. The aerodynamic coefficients of the dynamic cylinder differ significantly from those of the static cylinder. Therefore, it is concluded that performing a number of sequential steady-state computations would not yield adequate results for an unsteady flowfield around an object in relative motion near another object.

Acknowledgments

It was supported by Grant NAG-1-1150 from NASA Langley Research Center. The technical monitor for this work was David S. Miller.

References

[1]Baysal, O., Fouladi, K., Leung, R. W., and Sheftic, J. S., "Interference Flows Past a Cylinder-Fin-Sting-Cavity Assembly," *Journal of Aircraft*, Vol. 29, No. 2, 1992, pp. 194–202.

[2]Fouladi, K., and Baysal, O., "Viscous Simulation Method for Unsteady Flows Past Multicomponent Configurations," *ASME Journal of Fluids Engineering*, Vol. 114, No. 2, 1992, pp. 161–169.

[3]Baysal, O., and Yen, G. W., "Kinematic Domain Decomposition to Simulate Flows Past Moving Objects," AIAA Paper 91-0725, Jan. 1991.

[4]Kandil, O. A., and Chuang, H. A., "Computation of Vortex-Dominated Flow for a Delta Wing Undergoing Pitching Oscillation," *AIAA Journal*, Vol. 28, No. 9, 1990, pp. 1589–1595.

[5]Rausch, R. D., Batina, J. T., and Yang, H. T. Y., "Euler Flutter Analysis of Airfoils Using Unstructured Dynamic Meshes," *Journal of Aircraft*, Vol. 27, No. 3, 1990, pp. 436–443.

[6]Rumsey, C. L., and Anderson, W. K., "Some Numerical and Physical Aspects of Unsteady Navier-Stokes Computations over Airfoils Using Dynamic Meshes," AIAA Paper 88-0329, Jan. 1988.

[7]Thomas, J. L., Krist, S. T., and Anderson, W. K., "Navier-Stokes Computations of Vortical Flows Past Low Aspect Ratio Wings," *AIAA Journal*, Vol. 28, No. 2, 1990, pp. 205–212.

[8]Baysal, O., Yen, G. W., and Fouladi, K., "Navier-Stokes Computations of Cavity Aeroacoustics with Suppression Devices," *Proceedings of DGLR/AIAA 14th Aeroacoustics Conference* (Germany), 1992, pp. 940–948; also *ASME Journal of Vibration and Acoustics*, Vol. 116, No. 1, 1994, pp. 105–112.

[9]Baysal, O., Fouladi, K., and Lessard, V. R., "Multigrid and Upwind Viscous Flow Solver on 3-D Overlapped and Embedded Grids," *AIAA Journal*, Vol. 29, No. 6, 1991, pp. 903–910.

[10]Van Leer, B., "On Numerical Dispersion by Upwind Differencing," ICASE Report 86-18, Langley Research Center, Hampton, VA, March 1986, pp. 437–448.

[11]Ridder, J. P., and Beddini, R. A., "Temporal and Acoustic Accuracy of an Implicit Upwind Method for Ducted Flows," *AIAA Journal*, Vol. 29, No. 11, 1991, pp. 1860–1867.

[12]Steger, J. L., Dougherty, F. C., and Benek, J. A., "A Chimera Grid Scheme," *Advances in Grid Generation*, edited by K. Ghia and U. Ghia, Vol. 5, ASME-FED, New York, 1983, pp. 59–69.

[13]Meakin, R. L., and Suhs, N. E., "Unsteady Aerodynamic Simulation of Multiple Bodies in Relative Motion," AIAA Paper 89-1996, June 1989.

[14]Thomas, P. D., and Lombard, C. K., "The Geometric Conservation Law and its Application to Flow Computations on Moving Grids," *AIAA Journal*, Vol. 17, No. 10, 1979, pp. 1030–1037.

[15]Pulliam, T. H., "Characteristic Boundary Conditions for the Euler Equations," *Numerical Boundary Condition Procedures*, NASA-CP-2201, Moffet Field, CA, Oct. 1981, pp. 165–182.

[16]Landon, R., "NACA-0012 Oscillatory and Transient Pitching," *Compendium of Unsteady Aerodynamic Measurements*, AGARD Report 702, Neuilly sur Seine, France, Aug. 1982, pp. 3.3–3.25.